Abstract

Title of thesis: Droplet Dynamics in Microfluidic Expansions

Thomas K. Deskins, Master of Science, 2018

Thesis directed by: Professor Panagiotis Dimitrakopoulos
Department of Chemical and Biomolecular Engineering

In this thesis we conduct an investigation into the transient deformation of a droplet flowing through a sudden expansion in a microfluidic device. The dynamics of droplets in confined microfluidic geometries is a problem of fundamental interest as such flow conditions occur in multiphase flows in porous media, biological systems, microfluidics and material science applications. We computationally simulate naturally buoyant droplets possessing constant surface tension and of a size smaller than the cross-section of the rectangular channels in the expansion geometry. Our investigation presents cases in which the flow rate ranges from weak-to-strong and the fluids viscosity ratio ranges from low-to-high. The geometry of the expanding channel causes the droplet to display an interesting deformation behavior as it passes through the point of expansion. Our investigation draws attention to the effects of the asymmetric microchannel geometry on the droplet deformation and the different effects of the strength of the surrounding fluid flow rate, the fluid viscosity ratio, the initial displacement of the droplet, and the size of the droplet on the deformation of the droplet edges. In addition, our study highlights the multi-length nature of the current interfacial investigation.

Our investigation reveals that as the flow rate or the droplet size increases, the droplets show a rich deformation behavior as they moved inside the microfluidic channel. The viscosity ratio also has strong effects on the droplet deformation especially for high-viscosity droplets which do not have the time to accommodate the much slower deformation rate while they move through the channel. Our results

provide insight into the physical deformation of droplets flowing through microfluidic expansions.

Droplet Dynamics in Microfluidic Expansions

by

Thomas K. Deskins

Thesis submitted to the Faculty of the Graduate School of the
University of Maryland, College Park in partial fulfillment
of the requirements for the degree of
Master of Science
2018

Advisory Committee:

Professor Panagiotis Dimitrakopoulos, Chair/Advisor
Professor Amy J. Karlsson
Professor Jeffery B. Klauda

© Copyright by
Thomas K. Deskins
2018

Acknowledgments

I am grateful to the people that have helped me through my education and this thesis. To my father, Donald Deskins, for enduring long hours of work for decades to give me opportunity. His investment in my future has inspired me more than anything during my pursuit of an education and I cannot acknowledge his efforts enough.

To my friends, Andrew, Efe, Nick, and Shiv for all the support they have given me. To Professor Panagiotis Dimitrakopoulos for his support and guidance throughout my graduate studies. His expertise and directions made this work successful. To the members of our research lab, Abdollah Koolivand and Yiyang Wang. To my examining committee members, including Professors Amy J. Karlsson and Jeffery B. Klauda.

Further, I must acknowledge the Department of Chemical and Biomolecular Engineering at the University of Maryland, College Park.

Table of Contents

List of Figures iv

1 Introduction 1

1.1 Motivation for the Study of Droplet Motion 2

1.2 Review of Past Work 3

1.3 Overview of Present Research 4

2 Mathematical Formulation and Computational Method 8

2.1 Problem Description 8

2.2 Fluid Dynamics 11

2.3 Implicit Interfacial Spectral Boundary-Element Method 13

3 Results 17

3.1 Effect of Flow Rate 20

3.2 Effect of Viscosity Ratio 24

3.3 Effect of Droplet Size 29

3.4 Comparison between Straight Channel and Expansion 36

4 Conclusions 41

Bibliography 44

List of Figures

2.1 The microfluidic expansion used in our computations shown as (a) a schematic illustration and (b) a three-dimensional figure. 10

3.1 The shape of a droplet with radius $a/\ell_z = 0.5$, viscosity ratio $\lambda = 0.1$, capillary number Ca = 1.2, and initial displacement $z_c^0/\ell_z = 0.2$ at centroid $x_c/\ell_z = -2.86, -0.49, 1.73, 2.32, 3.64, 5.70$. (a) The droplet shape as seen from the negative y-axis (i.e front view). (b) As in (a) but as seen from the positive z-axis (i.e. top view). (c) The corresponding droplet profile (i.e. interfacial intersection with the plane $y = 0$) shown inside the microfluidic device. 18

3.2 Droplet lengths as a function of the centroid x_c, for a droplet with $a/\ell_z = 0.5$, $\lambda = 0.1$, $z_c^0/\ell_z = 0.2$ and Ca $= 0.3, 0.6, 0.9$. (a) Length L_x, (b) length L_y and (c) length L_z. 21

3.3 Evolution of droplet velocity U as a function of the centroid x_c, for a droplet with $a/\ell_z = 0.5$, $\lambda = 0.1$, $z_c^0/\ell_z = 0.2$ and Ca $= 0.3, 0.6, 0.9$. (a) U_x and (b) U_z. 23

3.4 Droplet displacement z_c as a function of the centroid x_c, for a droplet with $a/\ell_z = 0.5$, $\lambda = 0.1$, $z_c^0/\ell_z = 0.2$ and Ca $= 0.3, 0.6, 0.9$. 25

3.5 Droplet lengths as a function of the centroid x_c, for a droplet with $a/\ell_z = 0.5$, Ca $= 0.6$, $z_c^0/\ell_z = 0.2$ and $\lambda = 0.1, 1.0, 10$. (a) Length L_x, (b) length L_y and (c) length L_z. 27

3.6 Evolution of droplet velocity U as a function of the centroid x_c, for a droplet with $a/\ell_z = 0.5$, Ca $= 0.6$, $z_c^0/\ell_z = 0.2$ and $\lambda = 0.1, 1.0, 10$. (a) U_x and (b) U_z. 28

3.7 Droplet displacement z_c as a function of the centroid x_c, for a droplet with $a/\ell_z = 0.5$, Ca $= 0.6$, $z_c^0/\ell_z = 0.2$ and $\lambda = 0.1, 1.0, 10$. 30

3.8 Droplet lengths as a function of the centroid x_c, for a droplet with $\lambda = 0.1$, Ca $= 0.6$, $z_c^0/\ell_z = 0.2$ and $a/\ell_z = 0.1, 0.2, 0.3, 0.4, 0.5$. (a) Length L_x, (b) length L_y and (c) length L_z. 32

3.9 Evolution of droplet velocity U as a function of the centroid x_c, for a droplet with $\lambda = 0.1$, Ca $= 0.6$, $z_c^0/\ell_z = 0.2$ and $a/\ell_z = 0.1, 0.2, 0.3, 0.4, 0.5$. (a) U_x and (b) U_z. 34

3.10 Droplet displacement z_c as a function of the centroid x_c, for a droplet with $\lambda = 0.1$, Ca $= 0.6$, $z_c^0/\ell_z = 0.2$ and $a/\ell_z = 0.1, 0.2, 0.3, 0.4, 0.5$. . 35

3.11 The evolution of the profile for a droplet with $a/\ell_z = 0.5$, $\lambda = 0.1$, Ca $= 0.6$, and $z_c^0/\ell_z = 0.2$. (a) Droplet profile in a straight microchannel and (b) Droplet profile in the microfluidic expansion. . . . 37

3.12 Droplet lengths as a function of the centroid x_c, for a droplet with $a/\ell_z = 0.5$, $\lambda = 0.1$, Ca $= 0.6$ and $z_c^0/\ell_z = 0.2$. (a) Length L_x, (b) length L_y and (c) length L_z. 38

3.13 Evolution of the droplet velocity as a function of the centroid x_c, for a droplet with $a/\ell_z = 0.5$, $\lambda = 0.1$, Ca $= 0.6$ and $z_c^0/\ell_z = 0.2$ flowing in the microfluidic expansion or in a straight rectangular microchannel. (a) Translational velocity U_x and (b) migrational velocity U_z. 39

3.14 Droplet displacement z_c as a function of the centroid x_c, for a droplet with radius $a/\ell_z = 0.5$, $\lambda = 0.1$, Ca $= 0.6$ and $z_c^0/\ell_z = 0.2$. 40

Chapter 1

Introduction

In this paper we conduct an investigation into the transient deformation of a droplet flowing through a sudden expansion in a microfluidic device. We computationally simulate naturally buoyant droplets possessing constant surface tension and of a size smaller than the cross-section of the rectangular channels in the expansion geometry. Our investigation presents cases in which the flow rate ranges from weak-to-strong and the fluids viscosity ratio ranges from low-to-high. The geometry of the expanding channel causes the droplet to display an interesting deformation behavior as it passes through the point of expansion. Our investigation draws attention to the effects of the asymmetric microchannel geometry on the droplet deformation and the different effects of the strength of the surrounding fluid flow rate, the capillary number Ca, the fluid viscosity ratio λ, the initial displacement of the droplet z_c^0, and the size of the droplet a on the deformation of the droplet edges. In addition, our study highlights the multi-length nature of the current interfacial investigation.

A three-dimensional fully-implicit interfacial spectral boundary element method is used to determine the droplet dynamics in the expansions used in our computations. This problem is computationally challenging because it requires (i) a highly accurate stable numerical method to capture the interfacial evolution of the very

deformed droplets at high flow rates, large droplet sizes, large initial displacement values, and low viscosity ratios, and the close interaction between droplet and solid surfaces of the microfluidic channels, and (ii) an efficient algorithm for the complicated three-dimensional geometries of the microfluidic channels. In this chapter, we provide a description of the motivation for our research, a review of the past and current research, as well as an overview of our research on droplet dynamics in microfluidic channels with emphasis placed on expansions, described in detail in the following chapters.

1.1 Motivation for the Study of Droplet Motion

The study of the interfacial dynamics of droplets flowing in microscopic channels of varying geometries has allowed for the development of advanced microfluidic devices [49, 50]. Microfluidic devices employ channel configurations to best suit their needs in a wide range of applications. These applications include, but are not limited to, encapsulation of reactants with droplets acting as micro-reactors [46], improved drug delivery methods [58, 6], and direct contact heat/mass exchangers [35]. An attractive property of microfluidic devices is their ability to control the properties of small volumes of fluid. As such, many of these applications rely on that heightened sensitivity and need for controlled precision. Droplet-based microfluidics offers significantly reduced processing times and easy parallel processing, which allows for the acquisition of large data sets [4]. In addition, microfluidic devices can trap droplets and sort them based on the intrinsic physical characteristics of the droplet.

Fields that may not necessarily make use of microfluidics may require the understanding of the behavior and flow of non-wetting droplets in microscopic channels. In many biomedical processes, non-wetting droplets are used for sorting purposes. The applications of this is seen in personalized point-of-care diagnostic platforms, lab-on-a-chip systems, biochemical assays, and biosensors[4]. In other cases, such as in enhanced oil recovery, fluids flow through the underground porous media to displace trapped oil. The success of these operations depends on many factors, but the understanding of the multiphase flow is crucial [18]. The knowledge of the fundamental physics of droplets and bubbles in micro-channels is important in the lubrication process [40], the design and operation of fuel cells [32], and the delivery of drugs in vascular microvessels [55].

1.2 Review of Past Work

There has been much progress in understanding the deformation of a single droplet in shear and extensional flows. In the past, microfluidc expansions have been used to study bubble and droplet coalescence in conventional columns in different fluids [3]. The ability to controllably merge bubbles and droplets within segmented flow systems is applicable to many fields that make use of microfluidics [39]. Mazutis and Griffiths [34] presented an approach to selectively control droplet coalescence in a microfluidic expansion. Their results showed that the efficiency of droplet coalescence is dependent on the contact time between droplets and the interfacial surfactant coverage of droplets.

Many microfluidic devices combine microvalves and micropumps in order to achieve uni-directional species flow [53]. Valveless microvalves are ideally suited to high flow rates and high pressure conditions often found in microfluidic systems because they lack moving parts. Tsai and Lin [53] presented an approach that illustrates that sudden expansions in microfluidic devices can be used as valveless microvalves when used in conjunction with a solid structure blocking the main flow. This solid structure can act as a simple diffuser for forward flows that undergo expansion but cause flow vortices at large Reynolds numbers, defined below in equation 1.1, in reverse flows that undergo constriction.

$$\mathrm{Re} = \frac{\rho u L}{\mu} \tag{1.1}$$

This result shows that a flow rectification effect can be achieved without moving parts and with the sole use of a solid structure and a sudden expansion.

1.3 Overview of Present Research

In this paper, we examine the transient deformation of a droplet flowing through an expanding channel in a microfluidic device. These droplets possess constant surface tension and thus are naturally buoyant in the surrounding fluid occupying the continuous phase. The droplets in question vary in size but are smaller than the cross-section of the channels in the microfluidic device. Our investigation presents cases in which the flow rate ranges from weak-to-strong and the fluids viscosity ratio ranges from low-to-high.

Studying the motion and deformation of multi-phase particles like droplets in micro-channels provides vital information on their application and suitability to various fields. For example, understanding the stability of soft particle shapes provides insight to hydrodynamic aggregation and the effective viscosity of suspensions [2, 27]. As such, these studies play an important role in protein engineering, colloidal science, micro-reactors, fabrication of micro-particles, and lab-on-a-chip devices for clinical purposes.

Understanding the forces that determine the shape of a droplet in a microchannel is crucial in this investigation. The nonlinear coupling of the restoring interfacial forces and the deforming hydrodynamic forces of the flows are responsible for droplet deformation. As such, it can be seen that the droplet's transient conformational behavior strongly depends on the fluids viscosity ratio, the strength of the flow rate of the continuous phase, and the droplet's surface tension. Our investigation draws attention to the effects of the asymmetric microchannel geometry on the droplet deformation and the different effects of the strength of the surrounding flow rate, the fluid viscosity ratio, the initial displacement of the droplet, and the size of the droplet on the deformation of the droplet edges. In addition, our study highlights the multi-length nature of the current interfacial investigation.

Our microfluidic expansion is constructed from rectangular microfluidic channels. We release the naturally buoyant droplet, which is smaller than the cross-sectional area of the small rectangular channel, at various z_c^0 values off-center of the small rectangular channel. This droplet is released upstream of the expansion point. A three-dimensional fully-implicit spectral boundary element algorithm is

used to compute the droplet deformation and motion under Stokes flow condions in the microfluidic expansion. We compute the interfacial dynamics of the droplet from the time of its release until it reaches a point well downstream of the expansion. Our interest is on the investigation of the interfacial dynamics of the droplet as it flows through the sudden expansion point. In our computations, fluids are considered to be isothermal and Newtonian. We investigate the effects of flow rate, capillary number, droplet size, viscosity ratio, and initial displacement by studying the evolution of various geometric and physical parameters such as length, velocity, and displacement of the droplet.

In the next chapter, we will discuss the mathematical formulation of the problem, the expansion geometry and the computational method used.

In the following chapter, we will discuss the results of the experiment on the evolution of various parameters including length, velocity, and displacement of the droplet obtained from our computations in detail. Our work shows that the droplet dynamics in the expansion strongly depends on the flow rate, droplet size, viscosity ratio, and initial displacement of the droplet. As the flow rate, droplet size, or initial displacement of the droplet increases, the droplet shows a rich deformation behavior as it passes through the sudden expansion. Decreasing viscosity values show a similar effect on the deformation of the droplet. For low-viscosity droplets below $\lambda = O(1)$ the droplet deformation increases monotonically owing to higher inner hydrodynamic forces. For high-viscosity droplets with $\lambda = O(10)$, the droplet deformation decreases significantly as it passes through the expansion because the droplet does not have the time to accomodate the much slower deformation rate

compared to its fast movement.

In the final chapter, we will make detailed conclusions based on our results.

Chapter 2

Mathematical Formulation and Computational Method

2.1 Problem Description

A schematic diagram of the expansion employed in this work is shown in figure 2.1(a). The expansion is constructed from rectangular microfluidic channels. To facilitate our results description, we imagine that the main channel is the small channel on the left, as illustrated in figure 2.1(a). Thus the flow direction (*i.e.*, the x-axis) corresponds to the channel's or droplet's length, the z-direction will be referred as height while the y-direction will be referred as width (of the channel or the droplet). Seeing the droplet from the positive y-axis, positive z-axis or negative x-axis, represents a front view, a top view or an upstream view, respectively. In addition, we adopt the standard definition of geometric shapes (*e.g.* polygons). Thus we call the droplet's rear edge as convex when the radius of curvature at the middle of the rear edge points inside the capsule (*i.e.*, the local curvature is positive); in the opposite case the edge shape is concave. The half lengths of the rectangular cross-section of the main channel, along the y and z-axes are l_y and l_z respectively,

with $l_y = l_z = 1$. The origin of the system is placed at the point of expansion.

The droplet (fluid 1) with a density ρ_1 and viscosity $\lambda\mu$ is naturally buoyant in the surrounding fluid (fluid 2) with density ρ_2 and viscosity μ, as $\rho_1 = \rho_2$. The surface tension γ is assumed to be constant throughout the surface of the droplet. The undeformed spherical droplet, at the start of our computations, has a radius a with volume $V = \frac{4}{3}\pi a^3$. The incoming flow is upstream of the droplet. The undisturbed flow of fluid through the rectangular channel has an average velocity of $\mathcal{U}$.

In this study, if no scale is present, the channel's half-height l_z is used as the length scale, the velocity is scaled with the average undisturbed velocity $\mathcal{U}$, and thus time is scaled with $\tau_f = l_z/\mathcal{U}$. In addition the pressure is scaled with $\Pi = \mu\mathcal{U}/l_z$.

At the start of our computations the spherical droplet is placed inside the small channel upstream of the expansion. Due to the symmetry of the flow and the system, the droplet velocity in the direction of the y-axis is zero. As the droplet deforms, it moves horizontaly along the x-axis with additional movement in the z-direction. Due to the sudden expansion that the droplet passes through, the deformation varies to a greater degree than that of deformation of a droplet in a straight channel, under similar external shear and other physical conditions.

In this study, the major parameters of interest are the flow rate in the small channel, viscosity ratio, initial displacement of the droplet in the z-direction, and the size of the droplet. Figure 2.1(b) shows a three-dimensional view of the expansion.

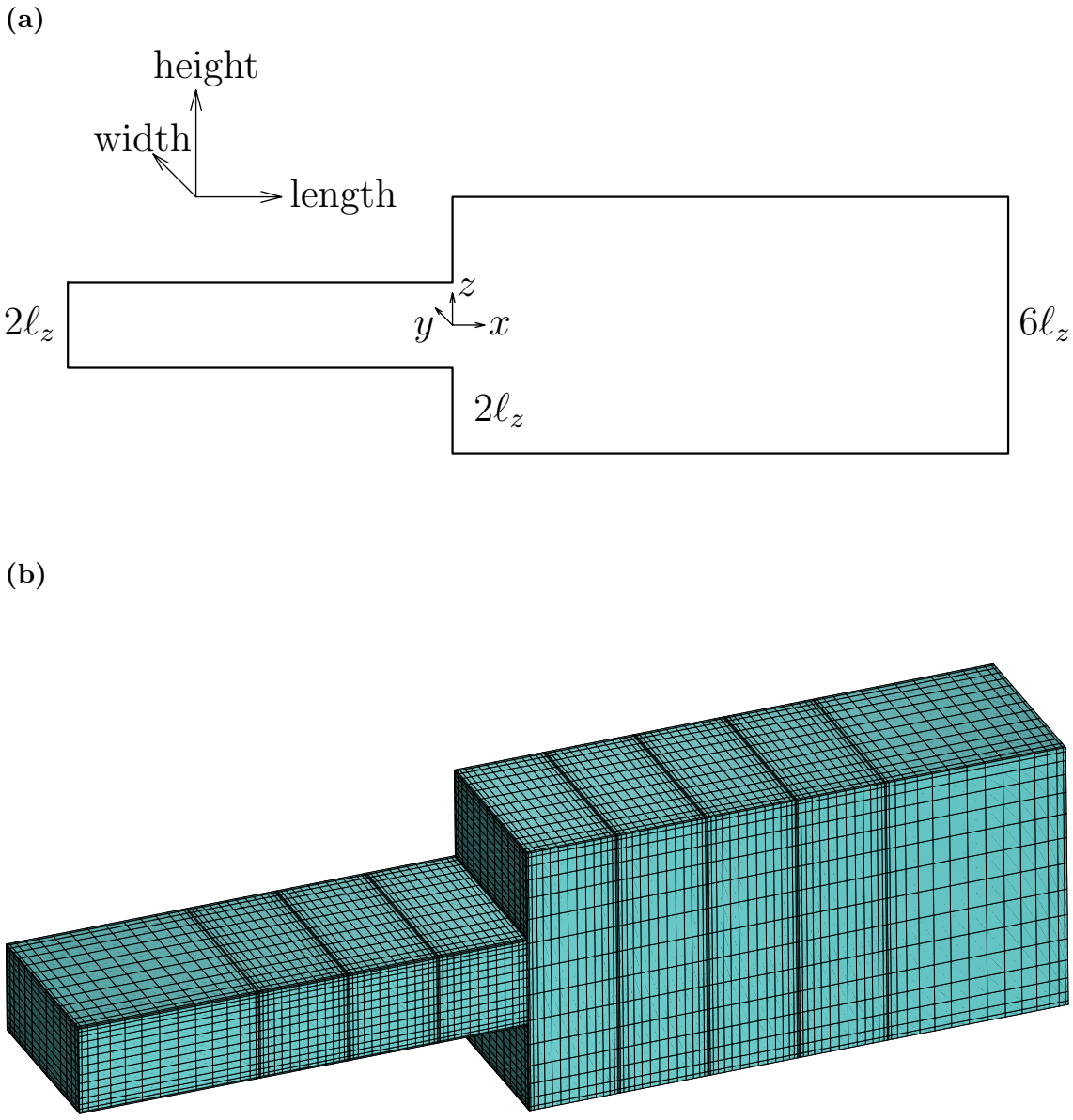


Figure 2.1: The microfluidic expansion used in our computations shown as (a) a schematic illustration and (b) a three-dimensional figure.

2.2 Fluid Dynamics

Due to the very small length scales involved with droplet flow in microfluidics junctions, the Reynolds number is very small and the inertial terms in the Navier-Stokes equations can be neglected. The flow is governed by Stokes equations

$$\nabla \cdot \boldsymbol{\sigma} \equiv -\nabla p + \mu \nabla^2 \boldsymbol{u} = 0 \tag{2.1}$$

and the continuity equation

$$\nabla \cdot \boldsymbol{u} = 0 \tag{2.2}$$

where $\boldsymbol{\sigma}$ is the stress tensor, p is the dynamic pressure and $\boldsymbol{u}$ is the velocity vector.

In this study, the system surface S_B consists of droplet surface S_d, the solid surface of the expansion S_s, the fluid surfaces S_f of the expansion. At the droplet surface the velocity is continuous and there is an interfacial stress jump owing to the surface tension. As the density of both fluids are same, the contribution of gravity to the interfacial stress jump is zero and thus the boundary conditions on the droplet surface are

$$\boldsymbol{u}_1 = \boldsymbol{u}_2 = \boldsymbol{u} \qquad \text{and} \qquad \Delta \boldsymbol{f} \equiv \boldsymbol{f}_2 - \boldsymbol{f}_1 = \gamma \nabla \cdot \boldsymbol{n} \tag{2.3}$$

Here the subscripts designate quantities related to the fluids 1 and 2 respectively, while $\boldsymbol{n}$ is the unit normal pointing from the droplet interface into fluid 2. The boundary conditions on the rest surfaces are

$$\boldsymbol{u} = 0 \qquad \text{on the solid boundary } S_s, \tag{2.4}$$

$$\boldsymbol{u} = \boldsymbol{u}^{\infty} \tag{2.5}$$

where $\boldsymbol{u}^{\infty}$ is the undisturbed channel velocity far from the droplet.

The undisturbed velocity profile for flow through a rectangular channel along x-axis, far from the droplet, can be found in the book by Yih [60], which is,

$$\frac{u^{\infty}(x)}{\Upsilon} = ({l_z}^2 - z^2) + \sum_{m=1}^{\infty} B_m \cosh(\frac{b_m y}{l_z}) \cos(\frac{b_m z}{l_z}), \tag{2.6}$$

where

$$\Upsilon = -\frac{1}{2\mu}, \quad b_m = \frac{(2m-1)\pi}{2}, \quad and$$
$$B_m = \frac{(-1)^m 4{l_z}^2}{{b_m}^3 \cosh(\frac{b_m {l_y}^2}{l_z})} \tag{2.7}$$

while p is the dynamic pressure. The volumetric flow rate Q can be obtained by integrating over the cross-section, which is,

$$\frac{Q}{\Upsilon} = \frac{8 l_y {l_z}^3}{3} + \sum_{m=1}^{\infty} B_m (\frac{2l_z}{b_m})^2 \sinh(\frac{b_m l_y}{l_z}) \sin(b_m) \tag{2.8}$$

Far from the droplet, the average velocity of the undisturbed flow is $\mathcal{U} = Q/(l_y\ l_z)$.

Based on standard boundary integral formulation, the velocity at a point $\boldsymbol{x}_0$ on the system surface S_B may be expressed as a surface integral of the force vector $\boldsymbol{f} = \boldsymbol{n} \cdot \boldsymbol{\sigma}$ and the velocity $\boldsymbol{u}$ over all points $\boldsymbol{x}$ on the boundary S_B,

$$\Omega \boldsymbol{u}(\boldsymbol{x}_0) = -\int_{S_d} [\boldsymbol{S} \cdot (\Delta \boldsymbol{f} - \mu(1-\lambda)\boldsymbol{T} \cdot \boldsymbol{u} \cdot \boldsymbol{n}]\,(\boldsymbol{x}) dS$$
$$- \int_{S_s \cup S_f} (\boldsymbol{S} \cdot \boldsymbol{f} - \mu \boldsymbol{T} \cdot \boldsymbol{u} \cdot \boldsymbol{n})(\boldsymbol{x}) dS \tag{2.9}$$

where the coefficient Ω takes values $4\pi\mu(1+\lambda)$ and $4\pi\mu$ for points $\boldsymbol{x}_0$ on the surfaces S_d and $S_s \cup S_f$ respectively. The tensors $\boldsymbol{S}$ and $\boldsymbol{T}$ are the fundamental

solutions for the velocity and stress for the three-dimensional Stokes equations, i.e., known functions of the system surface S_B [15]. For details the reader is directed to the textbook by Pozrikidis [41] or the article by Kuriakose and Dimitrakopoulos on the capsule motion inside a square microfluidic channel [26].

2.3 Implicit Interfacial Spectral Boundary-Element Method

The boundary integral equation, eq.(2.9), was solved using our three-dimensional implicit interfacial spectral boundary-element method. The boundary is divided into a number N_E of surface elements, each of which is parameterized by variables η and ξ on a square domain of $[-1, 1]^2$. The geometry and physical variables are discretized using Lagrangian interpolation in terms of these parametric variables. The number N_B of basis points (η_i, ξ_i) chosen for interpolation are zeros of orthogonal polynomials. Any point $\boldsymbol{x}$ on the geometry can be represented by

$$\boldsymbol{x}(\xi, \eta) = \sum_{i=1}^{N_B} \sum_{j=1}^{N_B} \boldsymbol{x}(\xi_i, \eta_i) h_i(\xi) h_j(\eta) \tag{2.10}$$

Similarly, the physical variables $\boldsymbol{u}$ and $\boldsymbol{f}$ can be interpolated at any point $\boldsymbol{x}$ from their values at the basis points.

Two types of points are used in solving the boundary integral equation by our spectral element method, the collocation points $\boldsymbol{x}_0$ where the equation is required to be satisfied and the basis points $\boldsymbol{x}$ where the physical variables $\boldsymbol{u}$ and $\boldsymbol{f}$ are specified. The collocation points $\boldsymbol{x}_0$ are of Legendre-Gauss quadrature where the points lie on the interior of the spectral elements. Thus the boundary integral equation is valid even at corners of singular elements. The basis points $\boldsymbol{x}$ are of

Legendre-Gauss-Lobatto quadrature and thus the physical variables are defined in the interior and edges of the spectral elements. Further details on the discretization of system surfaces can be found in these earlier papers [56, 17].

The transformation of the Stokes equations into boundary integral equations and their solution by an explicit time integration method has been a common method to determine the droplet shape as a function of time since the pioneering work of Acrivos and coworkers [61, 43]. This results in a great reduction in computational time as a three-dimensional problem can be described and solved using only two curvilinear coordinates. However, the explicit time integration requires a time step smaller than any time scale (numerical and physical) appearing in the problem. To ensure stability the time step employed has to satisfy the following condition,

$$\Delta t < O(Ca\ \Delta x_{min}) \tag{2.11}$$

where Δx_{min} is the minimum grid spacing in the computational problem [42, 63]. Dimitrakopoulos developed an efficient, fully implicit time-integration algorithm for interfacial dynamics in Stokes flow to avoid the computational cost associated with small time steps [17]. This method is based on a mathematically rigorous combination of implicit schemes with the Jacobian-free three-dimensional Newton method developed by Dimitrakopoulos and Higdon [15]. Both multi-step (one-stage) implicit formulae (e.g. Euler and backward differentiation schemes) and multi-stage diagonally implicit Runge-Kutta schemes are employed. By the combination of an implicit scheme with the Newton method, the interfacial algorithm preserves the stability properties of the corresponding implicit formula, and hence permits the

use of very large time steps. In addition, sufficient accuracy can be easily achieved, even with larger time steps, by employing high-order implicit schemes. In this work we use a third-order diagonally implicit Runge-Kutta scheme (DIRK3) with a time step $\Delta t = 10^{-2}$. Owing to the fully-implicit nature of our algorithm and the high-order DIRK3 scheme, even a larger time step $\Delta t = O(10^{-1})$ produces accurate results without causing interfacial breaking.

By combining the implicit interfacial method with the spectral boundary-element algorithm, the resulting algorithm exploits all the benefits of the spectral methods, i.e., high-order interpolation with exponential convergence and numerical stability with increasing number of spectral points, along with the versatility of the boundary-element method, i.e., the ability to handle the most complicated geometries. In addition, it is not affected by the disadvantage of the spectral methods used in volume discretization; namely the requirement to deal with dense systems, because in boundary-integral formulations the resulting systems are always dense and independent of the form of discretization. We note that the exponential convergence in the numerical accuracy is evident at both the properties of a given shape, such as the interfacial curvature, and the dynamic evolution of the interfacial shape. For more details the reader is directed to the article by Dimitrakopoulos [17].

In our study, the small channel is divided into four rows and the large channel, upstream of the point of expansion, is divided into five rows. Each row of the channels are represented by four surface elements, with one element representing a side of the row. Thus the solid walls of the expansion are divided into fifty elements. The droplet surface is divided in a minimum of six elements by cube projection, with

each element corresponding to a side of the cube. Our method is also capable of generating more surface elements on the droplet surface and more than one elements per row for each channel side. In most of our computations we have used ten surface elements for capturing the droplet shape. However for handling complex shapes of the deformed droplets for high Ca we have used up to 22 surface elements with progressive splitting of an element at the tip of the droplet into five elements. Such discretizations are not needed in most of the cases as the method is accurate, as shown from our convergence runs.

In most of our computations we utilized $N_B = 8$ basis points on each element. As we have N_E number of surface elements and ${N_B}^2$ points per spectral elements, we finally have a system of $3N_E{N_B}^2$ algebraic equations. For verification of accuracy of our results, we performed some runs with $N_B = 10$ basis points for moderate and high Ca and high droplet sizes a. The convergence runs showed that $N_B = 8$ is sufficient enough to capture the shape of the deformed droplets except for the cases with large Ca ($Ca = 0.4, 0.6$).

In all our computations carried out in this chapter, we exploited the symmetry level $y = 0$. Exploiting this symmetry reduces the memory requirements for storage of the system by a factor of 4^2, the computational time for calculating the system matrices by a factor of 2^2 and the solution time via direct system solvers by factor of 8^2.

Chapter 3

Results

The results obtained from the numerical computations are discussed in this chapter. We investigated a wide range of flow rates, viscosity ratios, droplet sizes, and initial displacement vaues and their effects on the length, velocity, and displacement of the studied droplet. The computations are performed on a spherical droplet placed in an undisturbed flow that deforms as it moves downstream. In our computations we typically fix any three of Ca, λ, a/ℓ_z, z_c^0/ℓ_z at Ca = 0.6, $\lambda = 0.1$, $a/\ell_z = 0.5$, $z_c^0/\ell_z = 0.2$ and vary the fourth over a wide range to study its effects on droplet motion and deformation. At the beginning of all computations, the droplet is placed off-center in the small channel at an initial displacement z_c^0/ℓ_z at the droplet centroid $x_c/\ell_z = -4$ and begins moving downstream due to flow initiation. We compute the droplet dynamics until the droplet centroid reaches $x_c/\ell_z = 8$. Our plots describe the entire range of droplet motion, but particular interest is given to the area around $x_c/\ell_z = 0$ where the sudden expansion occurs. Due to varying flow rates, we plot the results as a function of the droplet centroid scaled with the half-height of the channel x_c/ℓ_z instead of time.

Three-dimensional shapes of a droplet at different locations x_c are shown in figure 3.1(a,b). The three-dimensional views presented here were derived from the

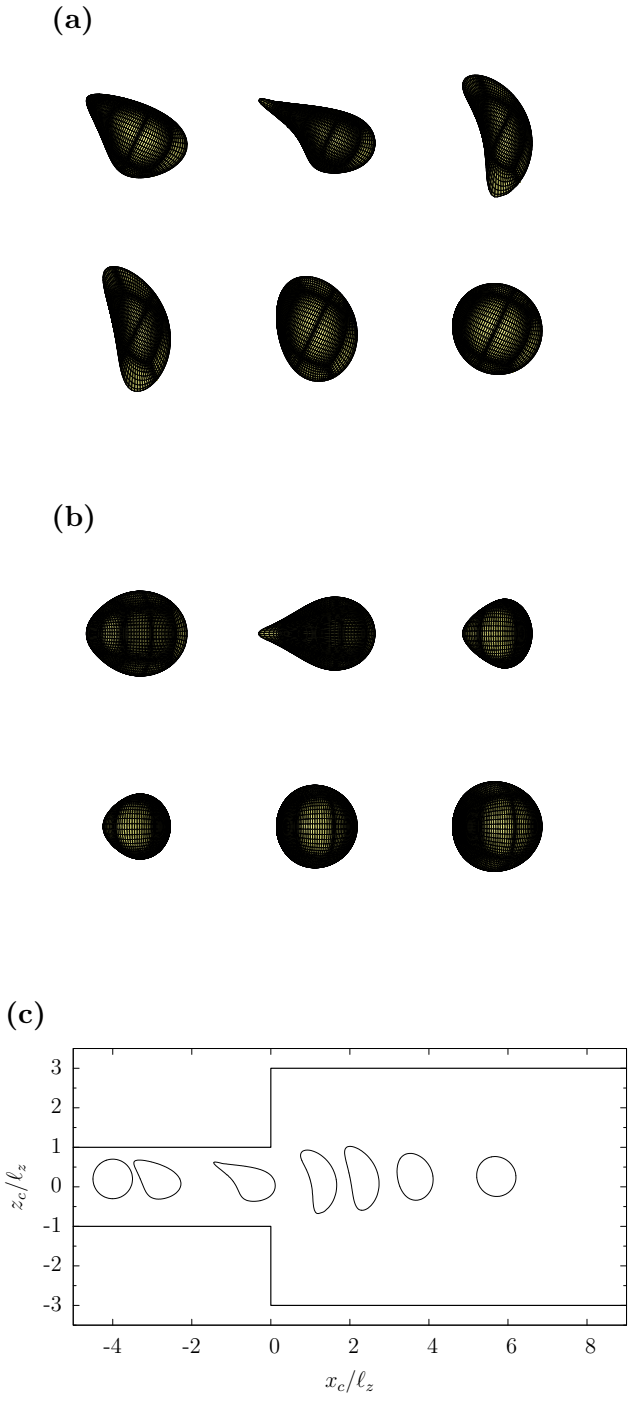


Figure 3.1: The shape of a droplet with radius $a/\ell_z = 0.5$, viscosity ratio $\lambda = 0.1$, capillary number $\mathrm{Ca} = 1.2$, and initial displacement $z_c^0/\ell_z = 0.2$ at centroid $x_c/\ell_z = -2.86, -0.49, 1.73, 2.32, 3.64, 5.70$. (a) The droplet shape as seen from the negative y-axis (i.e front view). (b) As in (a) but as seen from the positive z-axis (i.e. top view). (c) The corresponding droplet profile (i.e. interfacial intersection with the plane $y = 0$) shown inside the microfluidic device.

actual spectral grid by spectrally interpolating to $N_B = 22$. Afer the start of computation, the droplet starts flowing downstream and deforms due to the hydrodynamic forces acting on it. The first shape shows the droplet after it undergoes minor deformation at $x_c/\ell_z = -2.86$. The droplet then develops a tail pointed toward the wall since the flow is strongest at the centerline, as seen in the second shape. The deformation the droplet undergoes is due to the droplet's attempt to balance the hydrodynamic forces and the surface tension forces acting upon it. This can be explained by putting an observer at the center of the droplet, assuming a static frame of reference for the observer. With a spherical droplet, the net surface tension force is zero. The surface tension force acting at a point on the droplet surface is inversely proportional to its radius of curvature and can be written as

$$F_\gamma \sim \frac{\gamma}{R} \tag{3.1}$$

Where R is the radius of curvature at the point on the droplet. As the droplet begins to form a tail, there is a net surface tension force on the droplet

$$F_\gamma \sim \gamma(\frac{1}{R_1} - \frac{1}{R_2}) \tag{3.2}$$

where R_1 and R_2 are the radius of curvatures of the center of the tip and the rear of the droplet. This quantity is positive as R_1 is smaller than R_2.

As the tail of the droplet enters the zone of expansion, the rear of the droplet becomes more concave and the droplet assumes a parabolic shape in an attempt to balance the hydrodynamic and surface tension forces it experiences. This behavior

can be seen in the transition from the second shape to the third shape of the droplet. After the droplet leaves the zone of expansion and adapts to the regular flow of the large channel, the droplet reassumes a spherical shape. At this point, the radius of curvature of the rear becomes negative and thus the net surface tension force on the droplet becomes

$$F_\gamma \sim \gamma(\frac{1}{R_1} + \frac{1}{R_2}) \tag{3.3}$$

3.1 Effect of Flow Rate

In this section, we collect our computational results studying the effects of varying flow rates. The flow rate is quantified by the use of the capillary number. Since the width of the large channel is three times greater than the width of the small channel, the capillary number characterizing the flow in the small channel is effectively three times smaller than the given capillary number. A spherical droplet with viscosity ratio $\lambda = 0.1$, size $a/\ell_z = 0.5$, and initial displacement $z_c^0/\ell_z = 0.2$ is placed upstream of the point of expansion at $x_c/\ell_z = -4$ and the capillary number Ca varies in the range [0.3-0.9]. From our computations we found that the droplet's deformation depends strongly on Ca with an increase in its length and height and a decrease in its width.

Figure 3.2 shows the droplet length L_x along the flow direction, width L_y along the y-axis, and height L_z along the z-axis as a function of the droplet centroid position x_c/ℓ_z. It is observed from figure 3.2(a) that the total length of the droplet

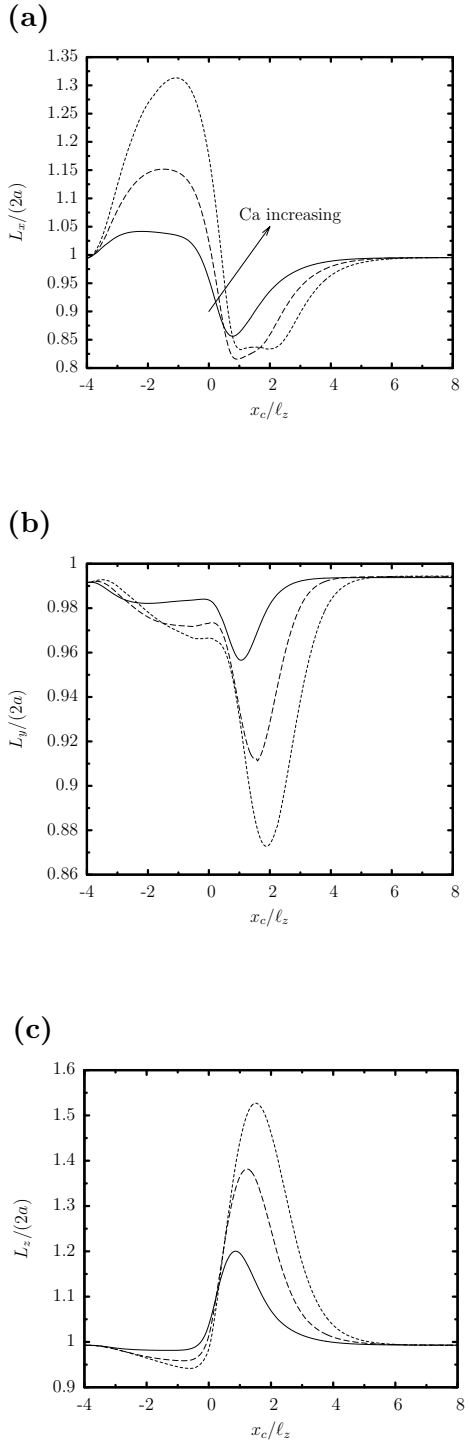


Figure 3.2: Droplet lengths as a function of the centroid x_c, for a droplet with $a/\ell_z = 0.5$, $\lambda = 0.1$, $z_c^0/\ell_z = 0.2$ and Ca $= 0.3, 0.6, 0.9$. (a) Length L_x, (b) length L_y and (c) length L_z.

L_x increases monotonically with an increase in flow rate. At first, the length L_x increases until the droplet reaches the zone of expansion at which the droplet sharply contracts in length. From figure 3.2(b) it can be seen that the droplet's width L_y slightly decreases with increasing flow rate as the droplet approaches the point of expansion. Similarly, from figure 3.2(c), the droplet's height L_z decreases with increasing flow rate as the droplet approaches the expansion point. These results are similar to the droplet deformation in low Reynold's number flows in a straight square channel [28, 57]. Lac *et al.*[28], in their study of droplets in a circular capillary, found that beyond a critical capillary number, droplets cannot attain steady state shapes, owing to capillary instability. We observed from our computations that this slightly occurs at high flow rates with Ca = 0.9. In addition, for the range of Ca studied in this chapter, none of the droplets break inside the channel.

Once the droplet passes through the point of expansion, the length and width of the droplet sharply drop while the height of the droplet sharply increases. The magnitude of this change increases with flow rate, as can be seen in figure 3.2(a,b,c). It should be noted that the droplet returns to a spherical shape for all the tested flow rates, as can be seen in the return of the scaled dimensions to a value of 1 as the droplet reaches steady state.

The velocity of the droplet for varying capillary numbers in both the x-direction and z-direction is plotted in figure 3.3 (a) and (b) against the droplet centroid x_c. The evolution of the velocity of the droplet in the x-direction shows that the initial velocity increase for large capillary numbers is ultimately insignificant. There is little difference in the droplet's flow velocity for varying capillary

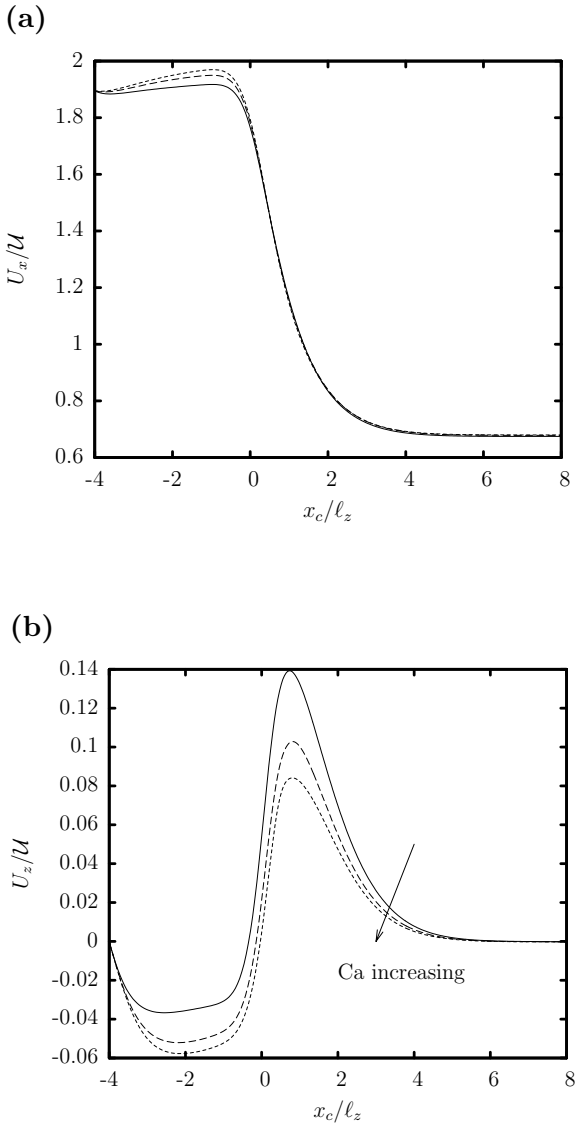


Figure 3.3: Evolution of droplet velocity U as a function of the centroid x_c, for a droplet with $a/\ell_z = 0.5$, $\lambda = 0.1$, $z_c^0/\ell_z = 0.2$ and $\mathrm{Ca} = 0.3, 0.6, 0.9$. (a) U_x and (b) U_z.

numbers. Figure 3.3(b) shows that the droplet initially moves toward the centerline at a faster rate for large capillary numbers. Similar behavior has been observed by Wang and Dimitrakopoulos in their study of microfluidic droplets in a straight rectangular channel [57]. The result is that the droplet is at a point closer to the centerline at the point of expansion for large capillary numbers. However, since the droplet is close to the centerline, it experiences a lesser corrective force in the positive z-direction for large capillary numbers, resulting in a lower velocity around $x_c/\ell_z = 1$ as the capillary number increases. Ultimately, the velocity reaches nearly 0 for all simulations at $x_c/\ell_z = 8$, indicating an approach to steady state.

Figure 3.4 shows the displacement of the droplet for varying capillary numbers in the z-direction. In each simulation, the droplet begins at a value of $z_c^0/\ell_z = 0.2$. In a general case, the droplet moves toward the centerline until it enters the zone of expansion. At that point, the droplet moves away from the centerline due to the effect of hydrodynamic forces. For large capillary numbers, the droplet initially moves closer toward the centerline but after the point of expansion does not migrate as much as the droplet with a small capillary number. Each simulation reaches a near-steady state.

3.2 Effect of Viscosity Ratio

In this section, we collect our computational results studying the effects of varying viscosity ratios on a droplet with size $a/\ell_z = 0.5$, capillary number Ca = 0.6, and initial displacement $z_c^0/\ell_z = 0.2$. The droplet is initially placed at $x_c/\ell_z = -4$ and

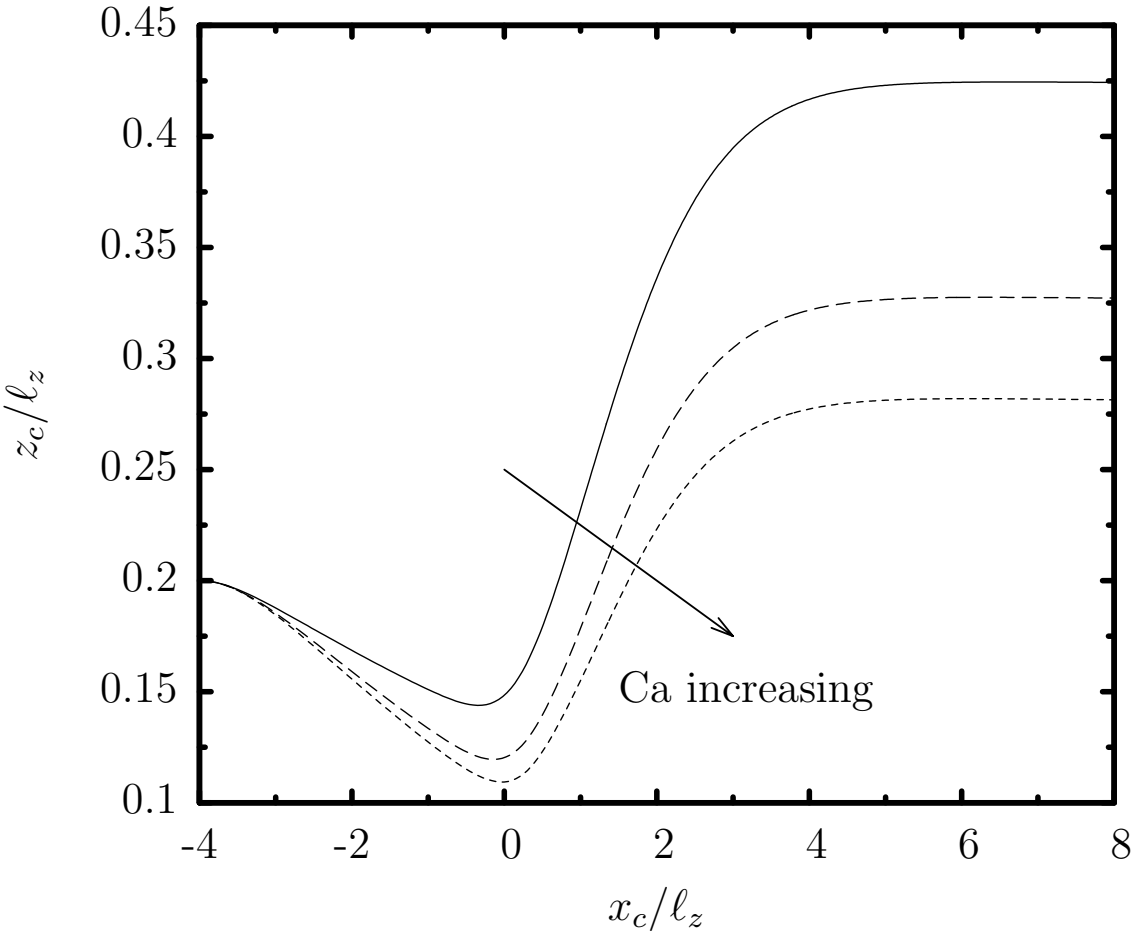


Figure 3.4: Droplet displacement z_c as a function of the centroid x_c, for a droplet with $a/\ell_z = 0.5$, $\lambda = 0.1$, $z_c^0/\ell_z = 0.2$ and $\mathrm{Ca} = 0.3, 0.6, 0.9$.

the viscosity ratio λ ranges with values of $\lambda = 0.1, 1, 10$. From our computations we found that the droplet's deformation depends strongly on λ with an increase in its length and height and a decrease in its width.

Figure 3.5 shows the droplet length L_x along the flow direction, width L_y along the y-axis, and height L_z along the z-axis as a function of the droplet centroid position x_c/ℓ_z. It is observed from figure 3.5 that the dimensions of the droplet vary wildly with varying viscosity ratios of the fluids. At high viscosity ratios, the droplet experiences less deformation than the droplet with $\lambda = [0.1, 1]$. In the case of a single droplet in a rectangular straight channel, it has been observed that the steady state deformation of the droplet increases with an increase in λ due to an increase in inner hydrodynamic forces [57]. However deformation takes place more slowly for a droplet with a higher λ, *i.e.*, a more viscous droplet needs more time deforming from its initial shape. The time needed for a droplet to deform can be expressed as

$$\tau \sim (1 + \lambda) Ca \, \tau_f \tag{3.4}$$

As such, the droplet with a high viscosity ratio also takes a longer time to return to a steady state value, as can be seen in figure 3.5. Once the droplet passes through the point of expansion, it returns to a spherical shape, as can be seen in the return of the scaled dimensions to a value of nearly 1 as the droplet reaches steady state.

The velocity of the droplet for varying viscosity ratios is plotted in figure 3.6 (a)

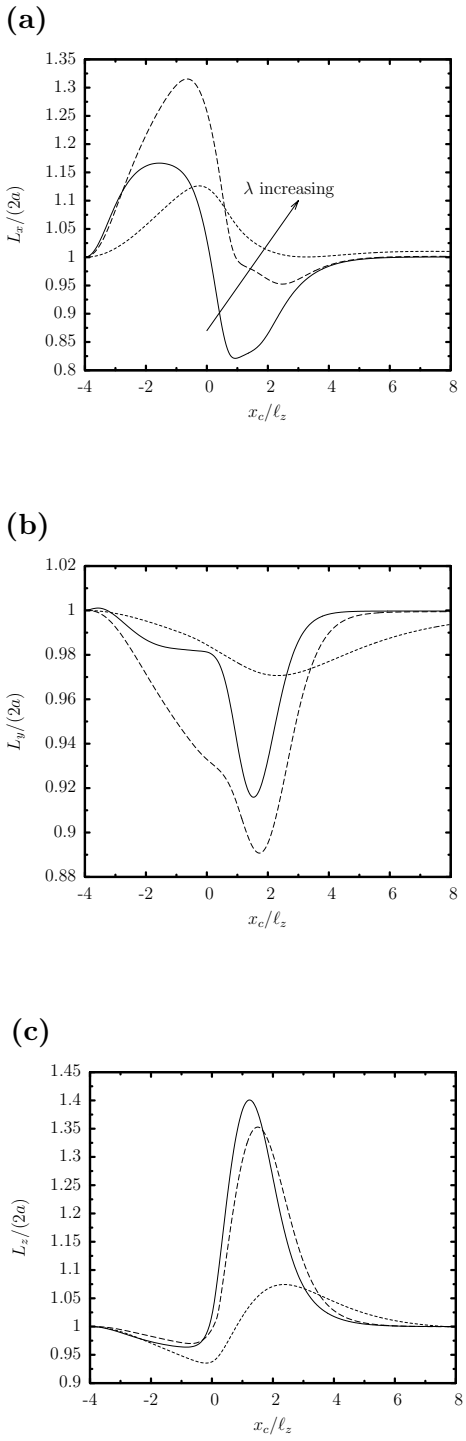


Figure 3.5: Droplet lengths as a function of the centroid x_c, for a droplet with $a/\ell_z = 0.5$, Ca $= 0.6$, $z_c^0/\ell_z = 0.2$ and $\lambda = 0.1, 1.0, 10$. (a) Length L_x, (b) length L_y and (c) length L_z.

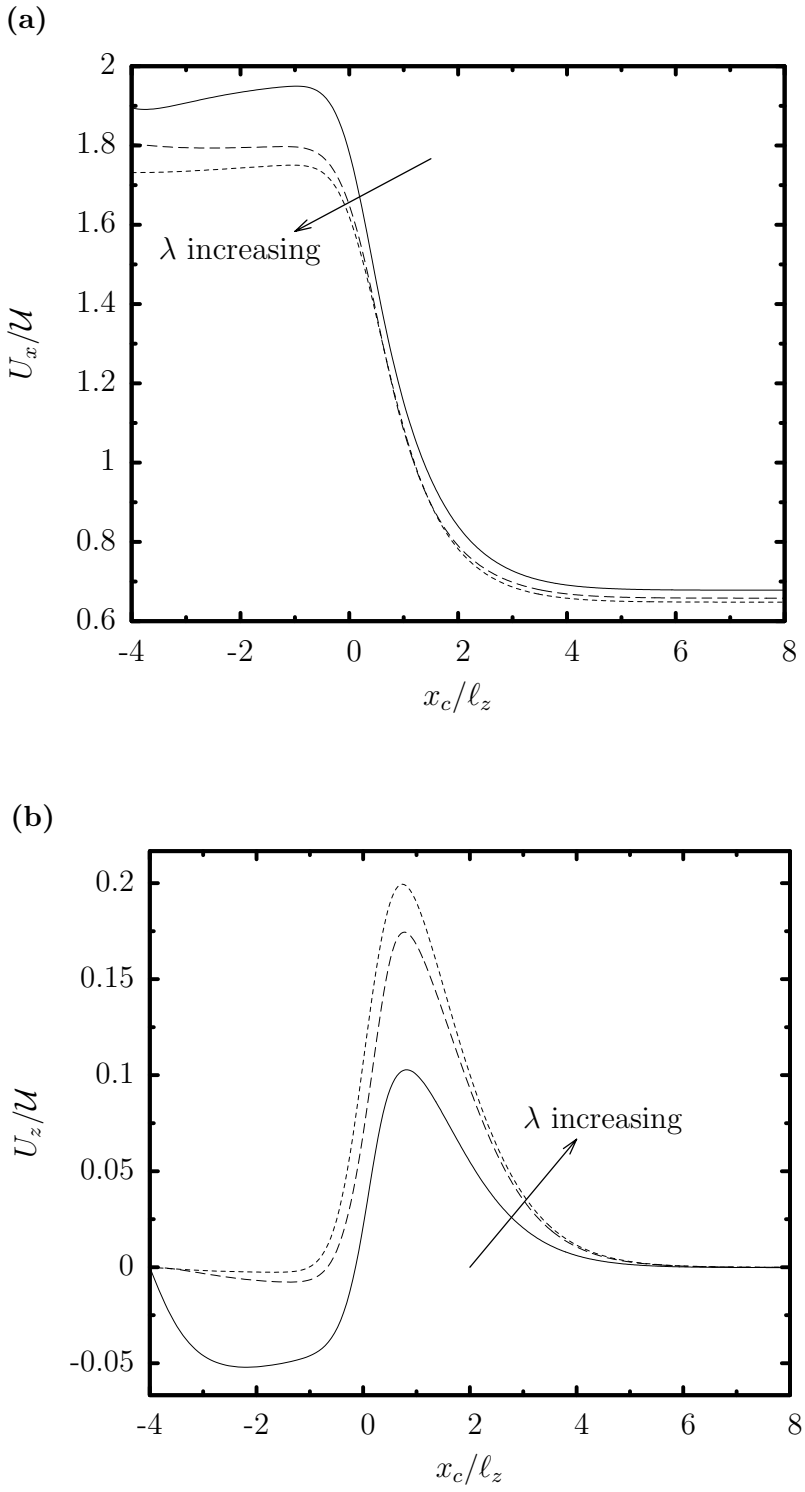


Figure 3.6: Evolution of droplet velocity U as a function of the centroid x_c, for a droplet with $a/\ell_z = 0.5$, Ca $= 0.6$, $z_c^0/\ell_z = 0.2$ and $\lambda = 0.1, 1.0, 10$. (a) U_x and (b) U_z.

and (b) against the droplet centroid x_c. The evolution of the velocity of the droplet in the x-direction shows that the droplet moves at a slower rate for increasing viscosity ratios. Figure 3.6(b) shows that the droplet initially moves toward the centerline at a faster rate for small viscosity ratios. The droplet with $\lambda = 0.1$ specifically shows strong migration toward the centerline. However, since the droplet is close to the centerline, it experiences a lesser corrective force in the positive z-direction for small viscosity ratios, resulting in a lower velocity around $x_c/\ell_z = 1$ as the viscosity ratio decreases. Ultimately, the velocity in the z-direction reaches nearly 0 for all simulations at $x_c/\ell_z = 8$, indicating an approach to steady state.

Figure 3.7 shows the displacement of the droplet for varying viscosity ratios in the z-direction. In each simulation, the droplet begins at a value of $z_c^0/\ell_z = 0.2$. In a general case, the droplet moves toward the centerline until it enters the zone of expansion. At that point, the droplet moves away from the centerline due to the effect of hydrodynamic forces. For small viscosity ratios, and especially for $\lambda = 0.1$, the droplet initially moves closer toward the centerline but after the point of expansion does not migrate as much as the droplet with a large viscosity ratio. Each simulation reaches a near-steady state.

3.3 Effect of Droplet Size

In this section, we collect our computational results studying the effects of varying droplet size on a droplet with viscosity ratio $\lambda = 0.1$, capillary number $\mathrm{Ca} = 0.6$, and initial displacement $z_c^0/\ell_z = 0.2$. The droplet is initially placed at $x_c/\ell_z = -4$

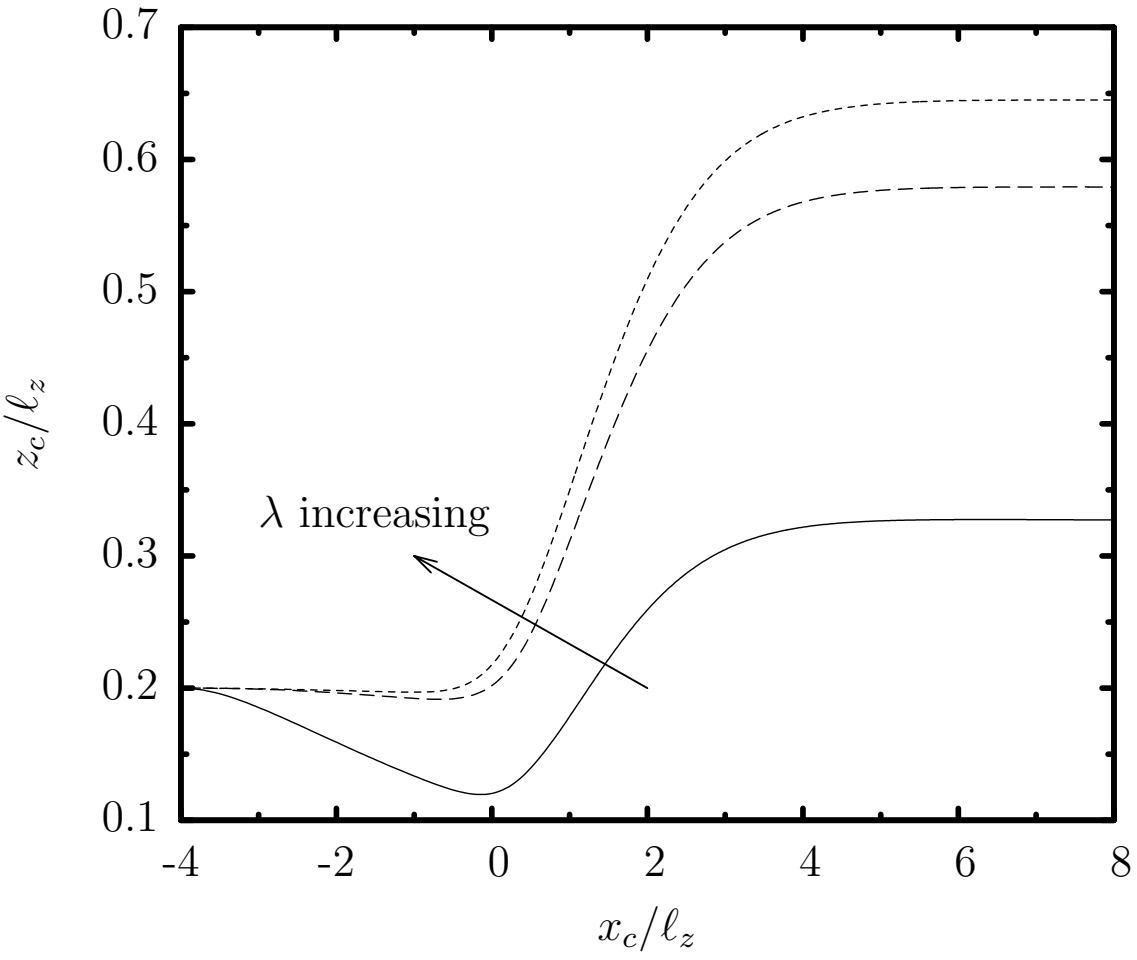


Figure 3.7: Droplet displacement z_c as a function of the centroid x_c, for a droplet with $a/\ell_z = 0.5$, Ca $= 0.6$, $z_c^0/\ell_z = 0.2$ and $\lambda = 0.1, 1.0, 10$.

and the droplet size a/ℓ_z ranges with values of $a = 0.1, 0.2, 0.3, 0.4, 0.5$. From our computations we found that the droplet's deformation depends on a with an increase in its height and a decrease in its width.

Figure 3.8 shows the droplet length L_x along the flow direction, width L_y along the y-axis, and height L_z along the z-axis as a function of the droplet centroid position x_c/ℓ_z. It is observed from figure 3.5 that the dimensions of the droplet vary with varying droplet sizes. In figure 3.8(a), the droplet length in the x-direction can be seen to initially increase, then suddenly decrease as the droplet enters the zone of expansion, then finally increase to nearly the steady state value of 1. The deformation increases as the size of the droplet increases. Similar behavior is shown for figure 3.8(b) in which the width of the droplet decreases at a faster rate for larger droplets. The opposite appears true for the height of the droplet, which increases more for larger droplets, as seen in figure 3.8(c).

For small droplets, there is little initial deformation. However, for moderately-sized and large droplets, there is substantial initial deformation. This is due to the large surface area which allows the hydrodynamic forces acting on the droplet to have an increased impact on the droplet and disturbance on the surface tension force, causing an increase in deformation. It is to be noted that the droplet deformation, and thus its length L_x, increases significantly with an increase in the droplet size. This is due to the fact that due to the large size of the droplet, the effective capillary number acting on the droplet becomes,

$$Ca^{\text{eff}} \sim \frac{\mu U}{\gamma}(\frac{L_z}{h})^n \tag{3.5}$$

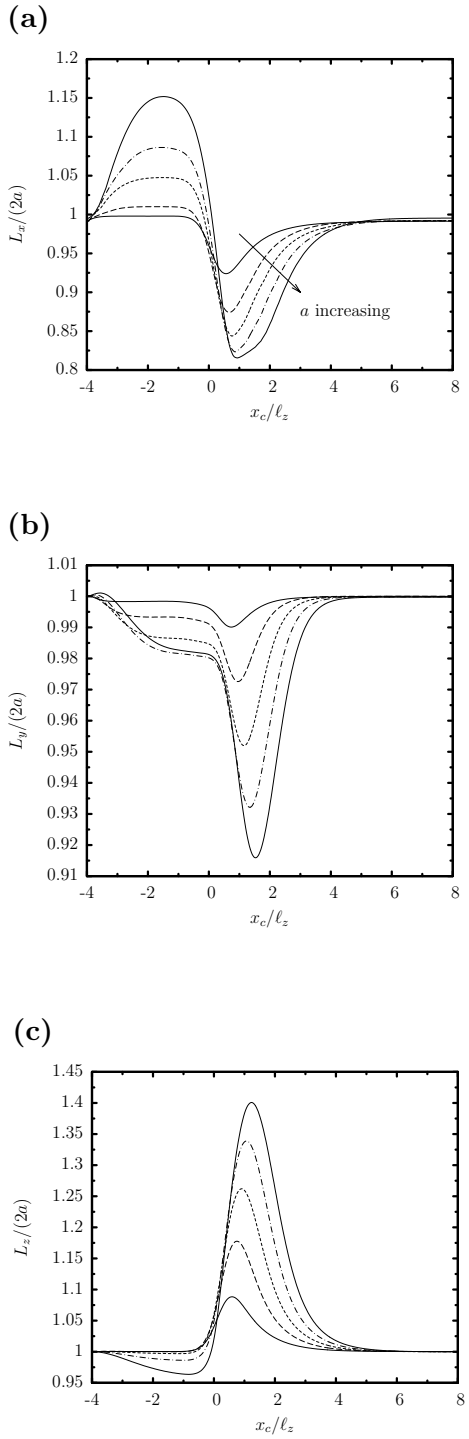


Figure 3.8: Droplet lengths as a function of the centroid x_c, for a droplet with $\lambda = 0.1$, Ca $= 0.6$, $z_c^0/\ell_z = 0.2$ and $a/\ell_z = 0.1, 0.2, 0.3, 0.4, 0.5$. (a) Length L_x, (b) length L_y and (c) length L_z.

due to the stronger hydrodynamic forces in the small gap h, where L_z is the length of the droplet along the z-axis. For the moderately sized droplets the factor $(\frac{L_z}{h})^n$ is not significantly greater than 1, while for the larger sized droplets the factor is large as h, the distance of the droplet interface from the wall of the channel decreases with an increase in droplet size. This is because of the higher deformation of the larger sized droplets by becoming thinner and longer to preserve its volume, while allowing the surrounding fluid to flow through the channel.

The velocity of droplets varying in size is plotted in figure 3.9 (a) and (b) against the droplet centroid x_c. The evolution of the velocity of the droplet in the x-direction shows that large droplets initially move slightly slower, but increase in velocity as they approach the point of expansion. Figure 3.9(b) shows that large droplets initially moves toward the centerline at a faster rate than small droplets. However, since the droplet is close to the centerline, it experiences a lesser corrective force in the positive z-direction for large droplets, resulting in a lower velocity around $x_c/\ell_z = 1$ as the droplet size increases. Ultimately, the velocity in the z-direction reaches nearly 0 for all simulations at $x_c/\ell_z = 8$, indicating an approach to steady state.

Figure 3.10 shows the displacement of droplets of varying size in the z-direction. In each simulation, the droplet begins at a value of $z_c^0/\ell_z = 0.2$. In a general case, the droplet moves toward the centerline until it enters the zone of expansion. At that point, the droplet moves away from the centerline due to the effect of hydrodynamic forces. For large droplet sizes, the droplet initially moves closer toward the centerline but after the point of expansion does not migrate as much as a small

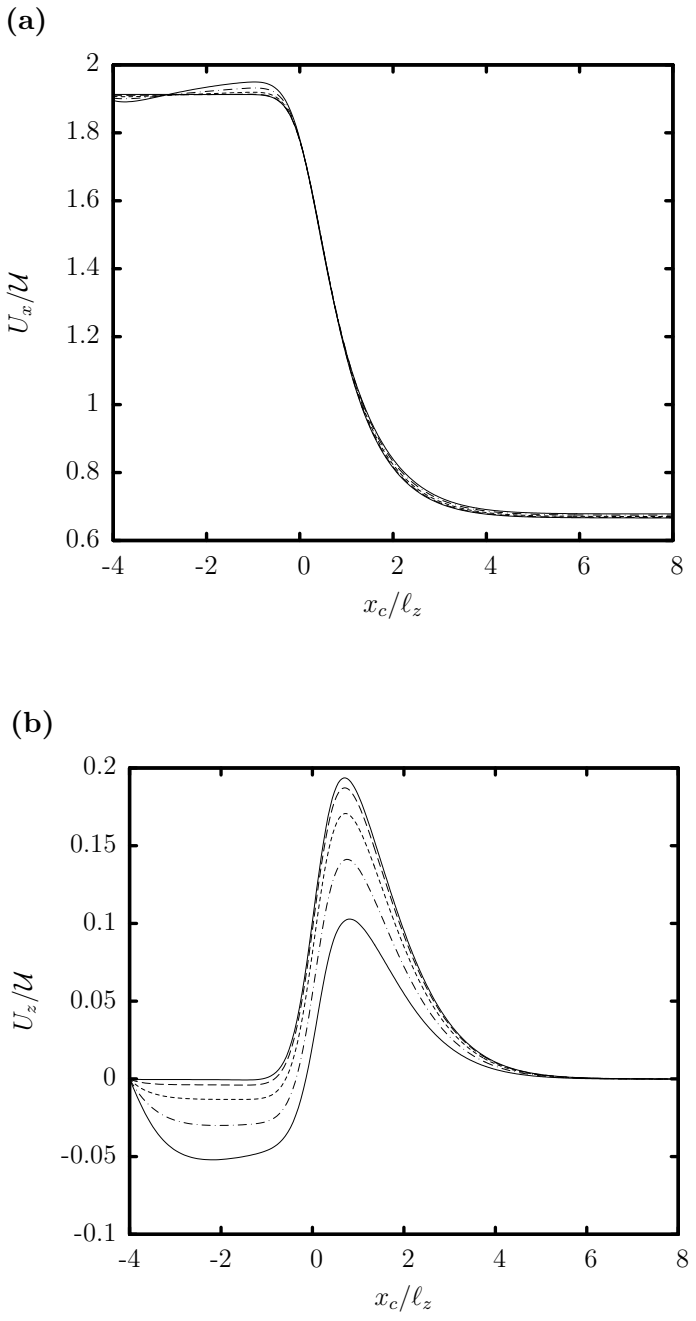


Figure 3.9: Evolution of droplet velocity U as a function of the centroid x_c, for a droplet with $\lambda = 0.1$, Ca $= 0.6$, $z_c^0/\ell_z = 0.2$ and $a/\ell_z = 0.1, 0.2, 0.3, 0.4, 0.5$. (a) U_x and (b) U_z.

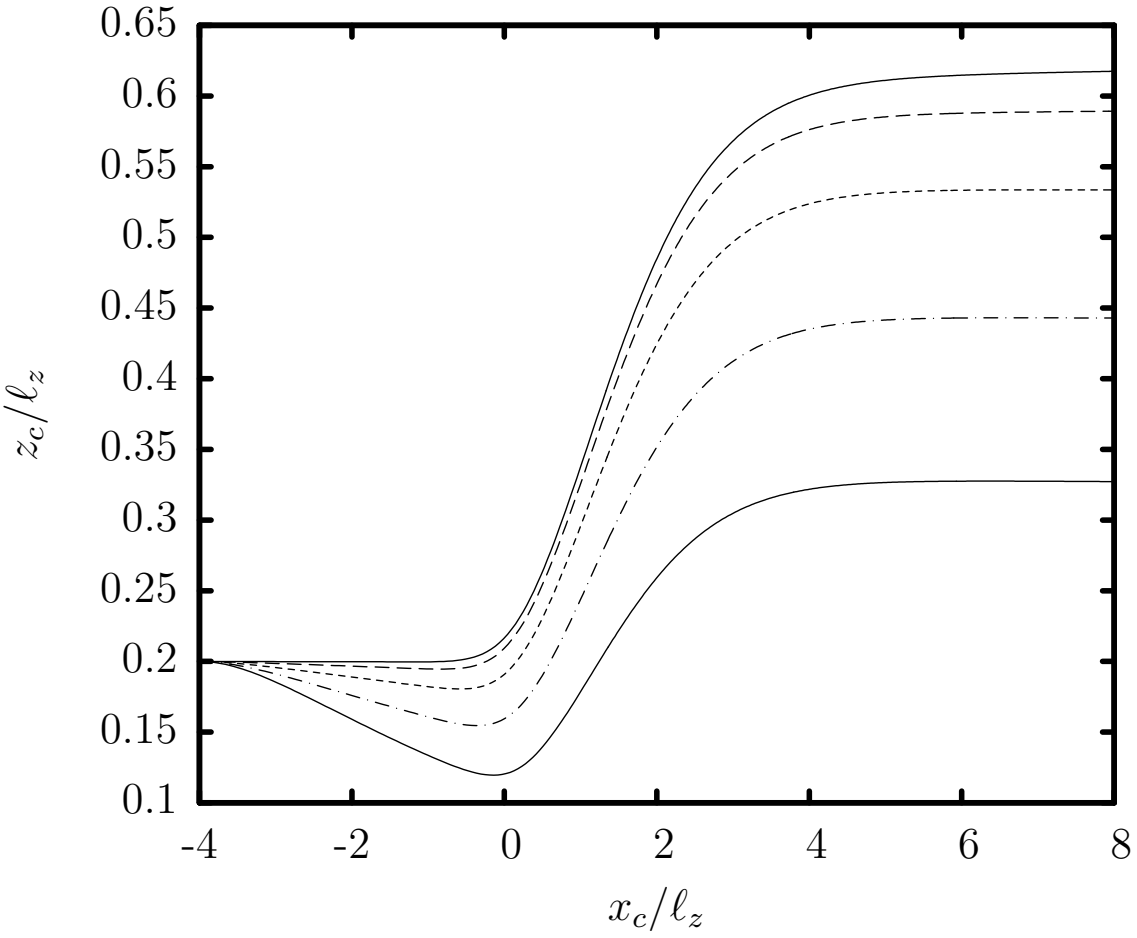


Figure 3.10: Droplet displacement z_c as a function of the centroid x_c, for a droplet with $\lambda = 0.1$, Ca $= 0.6$, $z_c^0/\ell_z = 0.2$ and $a/\ell_z = 0.1, 0.2, 0.3, 0.4, 0.5$.

droplet. Each simulation reaches a near-steady state.

3.4 Comparison between Straight Channel and Expansion

In this section, we provide figures that show how the microfluidic expansion differs from the well-studied straight rectangular channel. The intent of this is to illustrate that there is little difference between the droplet motion until the droplet reaches near the zone of expansion. In figure 3.11 we show the physical motion of the droplet through the use of the droplet profile.

Figure 3.12 shows the droplet dimensions over the droplet centroid in the expansion and the straight channel. Similar to the approach taken in other sections of this chapter, figure 3.13 shows the difference between the velocities in the channels, and figure 3.14 shows the difference between the droplet displacement over position for both channels.

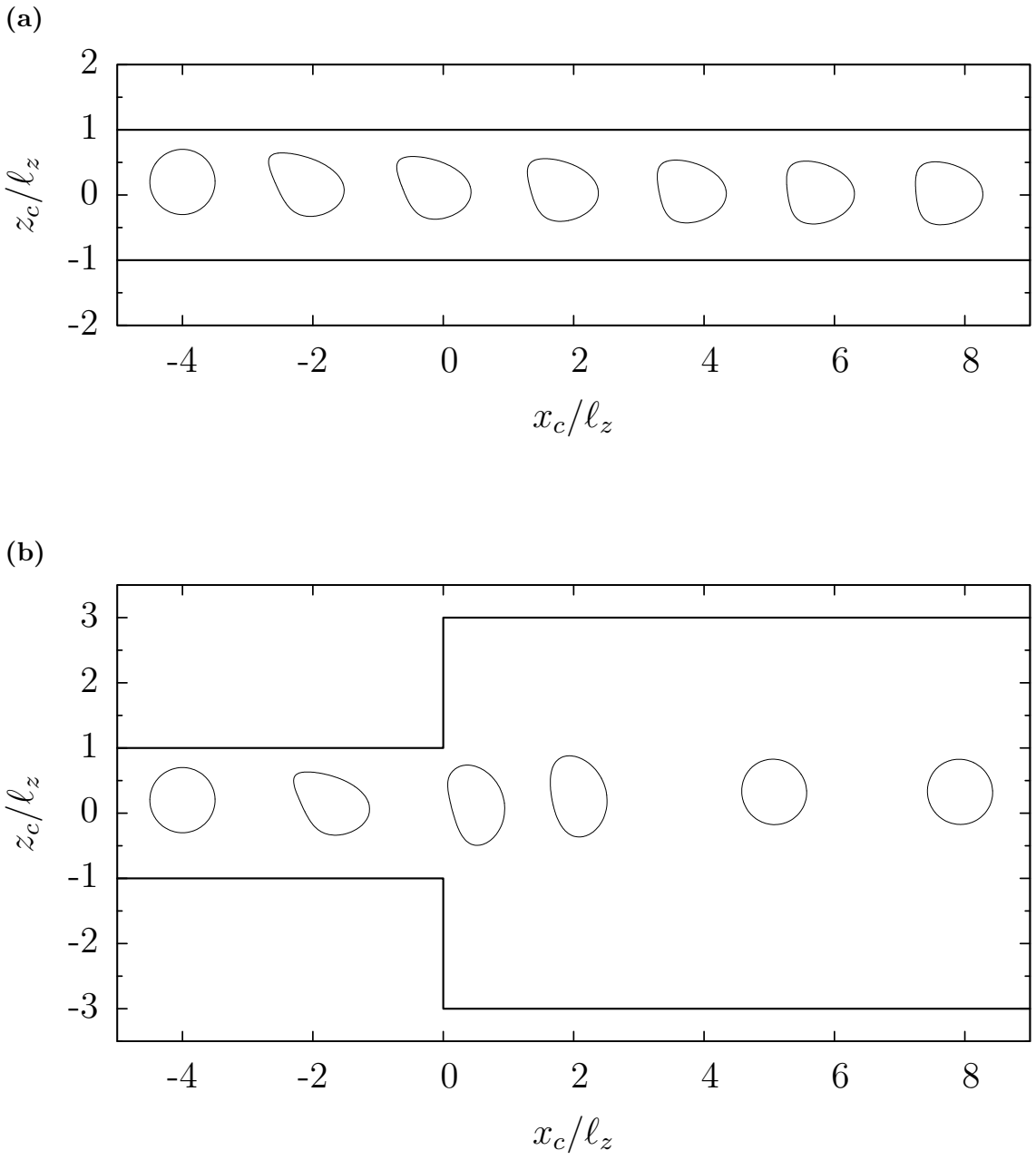


Figure 3.11: The evolution of the profile for a droplet with $a/\ell_z = 0.5$, $\lambda = 0.1$, Ca = 0.6, and $z_c^0/\ell_z = 0.2$. (a) Droplet profile in a straight microchannel and (b) Droplet profile in the microfluidic expansion.

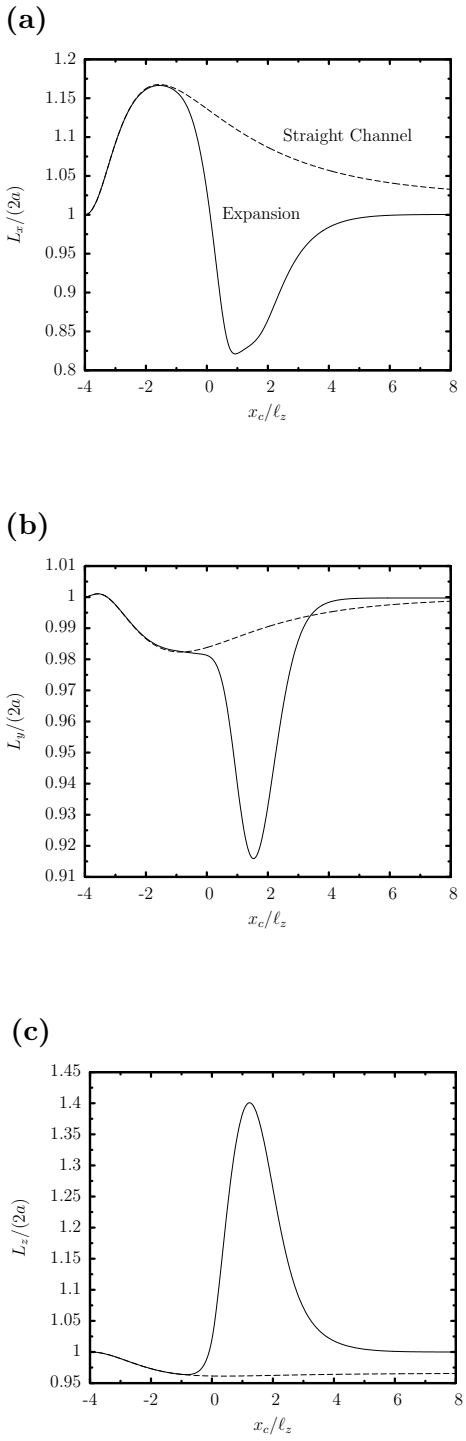


Figure 3.12: Droplet lengths as a function of the centroid x_c, for a droplet with $a/\ell_z = 0.5$, $\lambda = 0.1$, Ca $= 0.6$ and $z_c^0/\ell_z = 0.2$. (a) Length L_x, (b) length L_y and (c) length L_z.

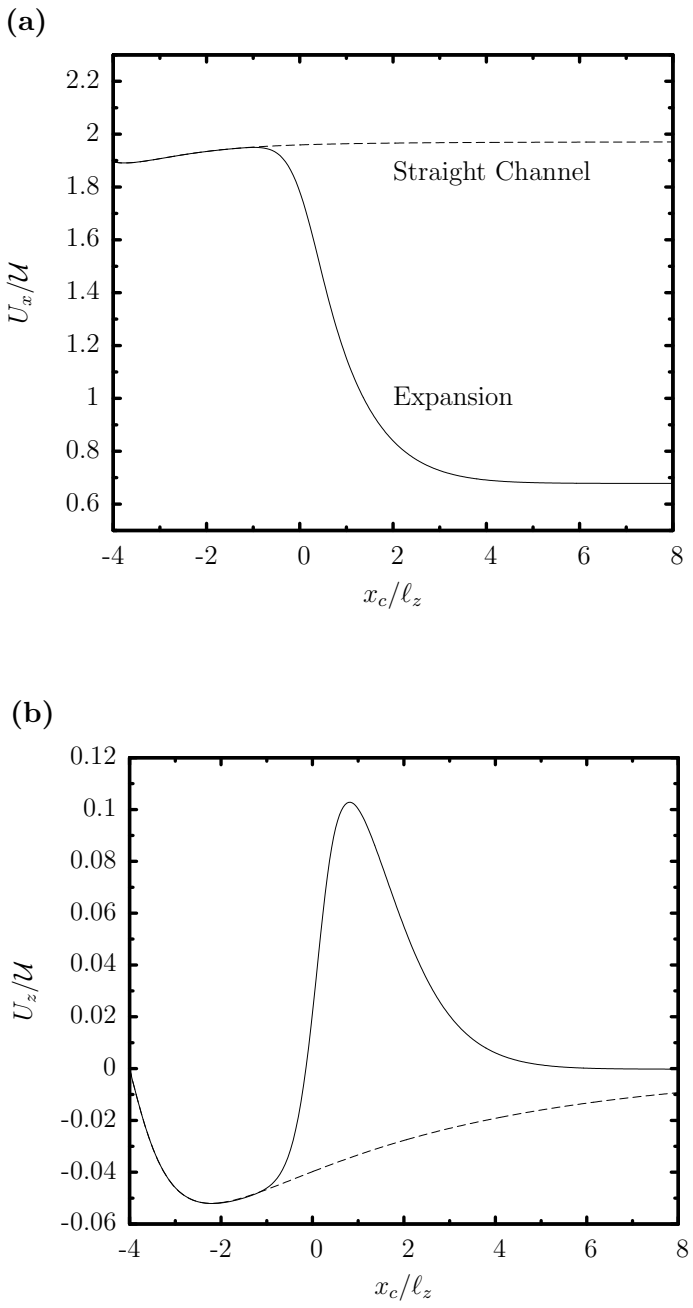


Figure 3.13: Evolution of the droplet velocity as a function of the centroid x_c, for a droplet with $a/\ell_z = 0.5$, $\lambda = 0.1$, Ca $= 0.6$ and $z_c^0/\ell_z = 0.2$ flowing in the microfluidic expansion or in a straight rectangular microchannel. (a) Translational velocity U_x and (b) migrational velocity U_z.

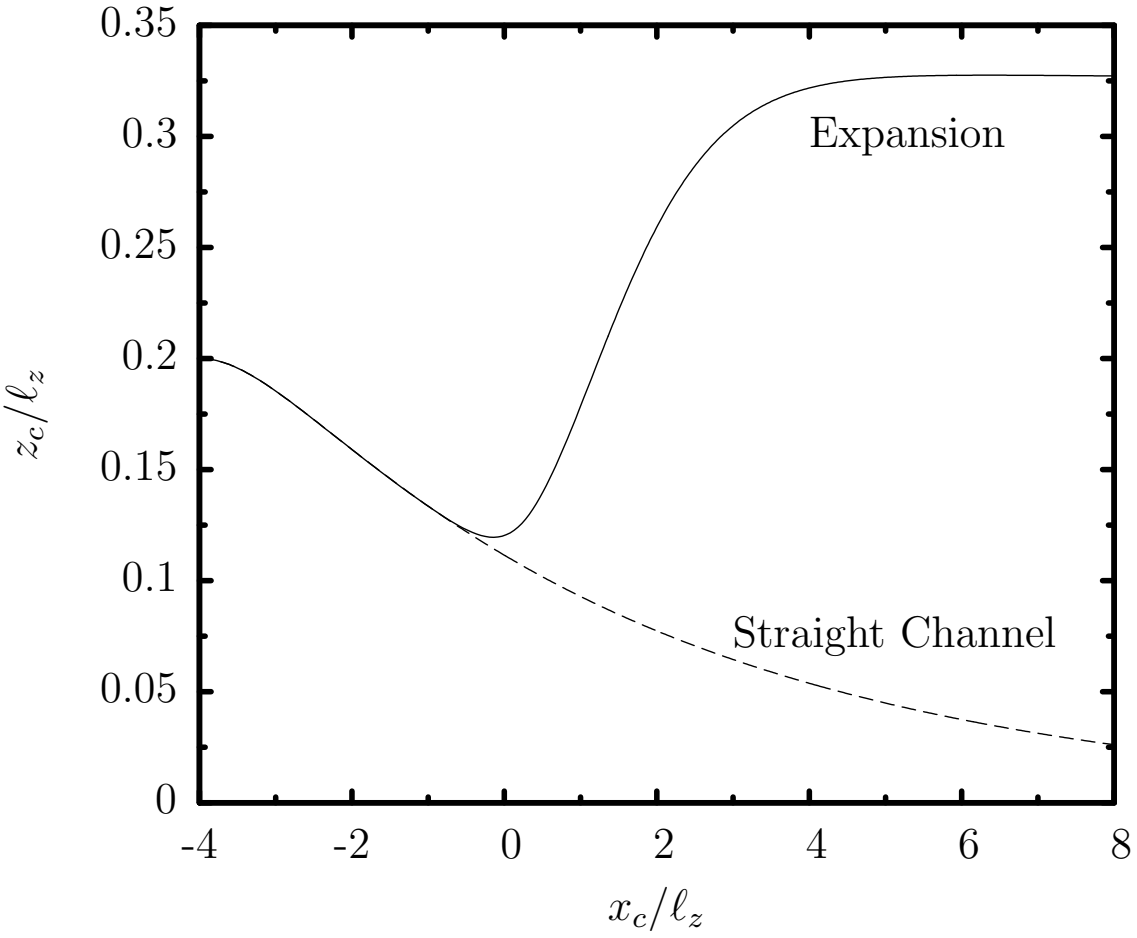


Figure 3.14: Droplet displacement z_c as a function of the centroid x_c, for a droplet with radius $a/\ell_z = 0.5$, $\lambda = 0.1$, Ca $= 0.6$ and $z_c^0/\ell_z = 0.2$.

Chapter 4

Conclusions

In this chapter, we have investigated computationally the dynamics of microfluidic droplets in a microfluidic expansion composed of rectagular channels. In particular, we have considered droplets with constant surface tension which are naturally buoyant in the surrounding fluid, and have size smaller than the cross-section of the rectangular channels comprising the device. The study is motivated by a wide range of applications including direct contact heat-mass exchangers, encapsulation of reactants with droplets as microreactors, drug delivery methods, coating processes, and of course applications in energy, e.g. enhanced oil recovery processes and direct methanol fuel cells.

To our knowledge, this is the first work to systematically study the dynamics of droplets, without interfacial breaking, in a microfluidic expansion device. Our investigations complement earlier studies on formation of droplets in a microfluidic expansion and droplet motion in a straight rectangular microfluidic channel [31, 57]. We summarize briefly some of the more important conclusions.

(i) Our computations investigating the effect of flow rate in a microfluidic expansion has revealed that the degree of interfacial deformation of the droplet, and hence its dynamics, depends on the strength of the flow in the device. In general,

upon release, the droplet deforms to assume a curved shape with its downstream tip pointed toward the center-line, so that to increase the restoring surface tension forces and thus balance the deforming hydrodynamic forces. When the droplet is complete in the zone of expansion, it becomes slender to due to the stronger hydrodynamic forces due to the sudden expansion and change in shear. As the droplet moves further downstream, the droplet centroid moves towards the tip of the droplet, as now its tail becomes pointed while the downstream tip becomes relatively less pointed. At flow rates high enough, the rear of the droplet may take a concave shape to balance the very strong hydrodynamic force with increased surface tension forces. As the droplet completely exits the zone of expansion, it gradually regains a spherical shape far downstream as it reaches steady state. It should be noted that the droplet returns to a spherical shape for all the tested flow rates, as can be seen in the return of the scaled dimensions to their initial value. During this diverse interfacial evolution, the droplet lengths, the droplet's velocity and its displacement in the z-direction change extensively, depending upon the droplet shape and location in the microfluidic device. We have monitored these parameters during the interfacial evolution of the droplet and have provided qualitative explanations.

(ii) We found that the viscosity ratio of the fluids strongly affect the dynamics of droplets in our expansion device. For high-viscosity droplets with $\lambda = O(10)$, the droplet deformation decreases significantly inside the expansion because the droplet does not have the time to accomodate the much slower deformation rate at high λ as it moves fast inside the microfluidic device. For low-viscosity droplets with $\lambda = O(10^{-1})$, the droplet deformation occurs quickly and can be seen in the wildly-

varying dimensions of the droplet. Since deformation takes place more slowly for a droplet with higher λ, the more viscous droplet requires more time to deform from its initial shape. As such, a droplet with a high viscosity ratio also takes longer to reach a steady state value.

(iii) By studying the effects of the droplet's sizes on its dynamics, we observed that the minimum distance of the droplet interface from the channel wall plays a significant role in its interfacial evolution. Large droplets show very apparent deformation. Before reaching the zone of expansion, the droplet develops a downstream tip pointed toward the centerline. For a large droplet, this tip is more pronounced due to the increased effect of the hydrodynamic forces on its large surface area. When the droplet is in the zone of expansion, the tip of the droplet becomes more pointed as it experiences deformation. The rear of the large droplets becomes concave due to the restoring forces. As the droplet leaves the zone of expansion, it begins to assume a spherical shape as it approaches steady state.

In addition, our study demonstrates the ability of our computational method to determine the droplet dynamics in intersecting flows accurately. With further modification in geometry, even more complicated droplet dynamics may be accurately predicted. Future work of this research could study more complex geometries under increasingly strenuous flow conditions to better model applications of this research.

Bibliography

[1] S. Afkhami, A. M. Leshansky and Y. Renardy, Numerical investigation of elongated drops in a microfluidic T-junction. *Phys. Fluids* **23**, 022002 (2011).

[2] V. S. Ajaev and G. M. Homsy, Modeling shapes and dynamics of confined bubbles. *Annu. Rev. Fluid Mech.* **38**, 277–307 (2006).

[3] N. Bao, Microfluidic electroporation of tumor and blood cells: observation of nucleus expansion and implications on selective analysis and purging of circulating tumor cells. *Integrative Biology* **2**, 113–120 (2010).

[4] C. N. Baroud, F. Gallaireb and R. Dangla, Dynamics of microfluidic droplets. *Lab. Chip.* **10**, 2032–2045 (2010).

[5] D. Barthès-Biesel and A. Acrivos, Deformation and burst of a liquid droplet freely suspended in a linear shear field. *J. Fluid Mech.* **61**(1), 1–21 (1973).

[6] J. A. Champion, Y. K. Katare and S. Mitragotri, Particle shape: a new design parameter for micro- and nanoscale drug delivery carriers. *J. Control. Release* **121**, 3–9 (2007).

[7] G. F. Christopher, J. Bergstein, N. B. End, M. Poon, C. Nguyen and S. L. Anna, Coalescence and splitting of confined droplets at microfluidic junctions. *Lab. Chip.* **9**, 1102–1109 (2009).

[8] G. F. Christopher, N. Nadia Noharuddin, Joshua A. Taylor, and Shelley L. Anna, Experimental observations of the squeezing-to-dripping transition in T-shaped microfluidic junctions. *Phys. Rev. E.* **78**, 036317 (2008).

[9] L. Clime, D. Brassard, and T. Veres, Numerical modeling of the splitting of magnetic droplets by multiphase lattice Boltzmann equation. *J. Appl. Phys.* **105**, 07B517 (2009).

[10] V. Cristini and Y. C. Tan, Theory and numerical simulation of droplet dynamics in complex flows-a review. *Lab. Chip.* **4**, 257–264 (2004).

[11] T. Cubaud, Deformation and breakup of high-viscosity droplets with symmetric microfluidic cross flows. *Phys. Rev. E.* **80**, 026307 (2009).

[12] T. Cubaud and C. Ho, Transport of bubbles in square microchannels *Phys. Fluids* **16**(12), 4575–4585 (2004).

[13] M. de Menech, P. Garstecki, F. Jousse and H. A. Stone, Transition from squeezing to dripping in a microfluidic T-shaped junction. *J. Fluid Mech.* **595**, 141–161 (2008).

[14] P. Dimitrakopoulos and J. J. L. Higdon, Displacement of fluid droplets from solid surfaces in low-Reynolds-number shear flows. *J. Fluid Mech.* **336**, 351–378 (1997).

[15] P. Dimitrakopoulos and J. J. L. Higdon, On the displacement of three-dimensional fluid droplets from solid surface in low-Reynolds-number shear flows. *J. Fluid Mech.* **377**, 189–222 (1998).

[16] P. Dimitrakopoulos and J. J. L. Higdon, On the displacement of three-dimensional fluid droplets adhering to a plane wall in viscous pressure-driven flows. *J. Fluid Mech.* **435**, 327–350 (2001).

[17] P. Dimitrakopoulos, Interfacial dynamics in Stokes flow via a three-dimensional fully-implicit interfacial spectral boundary element algorithm. *J. Comp. Phys.* **225**, 408–426 (2007).

[18] P. Dimitrakopoulos, Deformation of a droplet adhering to a solid surface in shear flow: onset of interfacial sliding. *J. Fluid Mech.* **580**, 451–466 (2007).

[19] M. M. Dupin, I. Halliday and C. M. Care, Simulation of a microfluidic flow-focussing device. *Phys. Rev. E.* **73**, 055701(R) (2006).

[20] P. Garstecki, M. J. Fuerstman, H. A. Stone and G. M. Whitesides, Formation of droplets and bubbles in a microfluidic T-junctions : scaling and mechanism of break-up. *Lab. Chip.* **6**, 437–446 (2006).

[21] H. Gu, M. H. G. Duits, F. Mugele, Droplet formation and merging in two-phase flow microfluidics. *Int. J. Mol. Sci.* **12**, 2572-2597 (2011).

[22] S. Guido, Shear-induced droplet deformation: Effects of confined geometry and viscoelasticity. *Current Opinion in Colloid and Interface Science* **16**, 61–70 (2011).

[23] D. J. E. Harvie, J. J. Cooper-White and M. R. Davidson, Deformation of a viscoelastic droplet passing through a microfluidic contraction. *J. Non-Newtonian Fluid Mech.* **155**, 67–79 (2008).

[24] W. B. Kolb, R. L. Cerro, Coating the inside of a capillary of square cross section. *Chem. Eng. Sci.* **46**, 2181–2195 (1991).

[25] W. B. Kolb, R. L. Cerro, The motion of long bubbles in tubes of square cross section. *Phys. Fluids A* **5**, 1549–1557 (1993).

[26] S. Kuriakose and P. Dimitrakopoulos, Motion of an elastic capsule in a square microfluidic channel. *Phys. Rev. E* **84**, 011906 (2011).

[27] S. Kuriakose and P. Dimitrakopoulos, Deformation of an elastic capsule in a retangular microfluidic channel. *Soft Matter* **9**, 4284–4296 (2013).

[28] E. Lac and J. D. Sherwood, Motion of a drop along the centerline of a capillary in a pressure-driven flow. *J. Fluid Mech.* **640**, 27–54 (2009).

[29] A. M. Leshansky, S. Afkhami, M.C. Jullien, and P. Tabeling, Obstructed breakup of slender drops in a microfluidic T junction. *Phys. Rev. Lett.* **108**, 264502 (2012).

[30] J. Liu and N.T. Nguyen, Numerical simulation of droplet-based microfluidics-A review. *Micro and Nanosystems* **2**(3), 193–201 (2010).

[31] H. Liu and Y. Zhang, Droplet formation in microfluidic cross-junctions. *Phys. Fluids* **23**, 082101 (2011).

[32] H. Liu and Y. Zhang, Electrochemical and flow characterization of a direct methanol fuel cell. *J. Power Sources* **134**, 33–40 (2004).

[33] J. Magnaudet, S. Tagaki and D. Legendre, Drag, deformation and lateral migration of a buoyant drop moving near a wall. *J. Fluid Mech.* **476**, 115–157 (2003).

[34] L. Mazutis, A. D. Griffiths, Selective droplet coalescence using microfluidic systems. *Lab. Chip.* **12**, 1800–1806 (2012).

[35] J. L. Mercier, F. M. da Cunha, J. C. Teixeira and M. P. Scofield, Influence of enveloping water layer on the rise of air bubbles in Newtonian fluids. *J. Appl. Mech.* **41**(1), 29–35 (1974).

[36] M. Minale, S. Caserta and S. Guido, Microconfined shear deformation of a droplet in an equiviscous non-Newtonian immiscible fluid: Experiments and modeling. *Langmuir* **26**(1), 126–132 (2011).

[37] M. K. Mulligan and J. P. Rothstein, Scale-up and control of droplet production in coupled microfluidic flow-focussing geometries. *Microfluid. Nanofluid.* **13**(1), 65–73 (2012).

[38] M. A. Nilsson, J. P. Rothstein, The effect of contact angle hysteresis on droplet coalescence and mixing *J. Colloid Interf. Sci.* **363** 646–654 (2011).

[39] X. Niu, Pillar-induced droplet merging in microfluidic circuits *Lab. Chip.* **8** 1837–1841 (2008)

[40] W. L. Olbricht, Pore-scale prototypes of multiphase flow in porous media *Ann. Rev. Fluid Mech.* **28** 187–213 (1996).

[41] C. Pozrikidis, Boundary integral and singularity methods for linearized viscous flow. Cambridge Texts In Applied Mathematics, (1992).

[42] J. M. Rallison, A numerical study of the deformation and burst of a viscous drop in general shear flows. *J. Fluid Mech.* **109**, 465–482 (1981).

[43] J. M. Rallison and A. Acrivos, A numerical study of the deformation and burst of a viscous drop in an extensional flow. *J. Fluid Mech.* **89**(1), 191–200 (1978).

[44] M. Shapira and S. Haber, Low Reynolds number motion of a droplet in shear flow including wall effects. *Int. J. Multiph. Flow* **16**, 305–321 (1990).

[45] X. C. Solvas and A. deMello, Droplet microfluidics: recent developments and future applications. *Chem. Commun.* **47**, 1936–1942 (2011).

[46] H. Song, J. D. Tice and R. F. Ismagilov, A microfluidic system for controlling reaction networks in time. *Angew. Chem. Int. Ed. Engl.* **42**(7), 768–772 (2003).

[47] F. Takemure, J. Magnaudet and P. Dimitrakopoulos, Migration and deformation of bubbles rising in a wall-bounded shear flow at finite Reynolds number. *J. Fluid Mech.* **634**, 463–486 (2009).

[48] Y. C. Tan, V. Cristini and A. P. Lee, Monodispersed microfluidic droplet generation by shear focusing microfluidic device. *Sensors and Actuators B: Chemical* **114**(1), 350–356 (2005).

[49] G. I. Taylor, The viscosity of a fluid containing small drops of another fluid *Proc. Roy. Soc. A* **138**, 41–48 (1932).

[50] G. I. Taylor, The formation of emulsions in definable fields of flow *Proc. Roy. Soc. A* **146**, 501–523 (1934).

[51] T. Thorsen, R. W. Roberts, F. H. Arnold and S. R. Quake, Dynamic Pattern Formation in a Vesicle-Generating Microfluidic Device. *Phys. Rev. Lett.* **86**(18), 4163-4166 (2001).

[52] T. M. Tsai and M. J. Miksis, Dynamics of a drop in a constricted capillary tube. *J. Fluid Mech.* **274**, 197–217 (1994).

[53] C. Tsai, C. Lin, L. Fu, and H. Chen, High-performance microfluidic rectifier based on sudden expansion channel with embedded block structure. *Biomicrofluidics* **6**(2), 024108 (2012).

[54] P. B. Umbanhowar, V. Prasad, and D. A. Weitz, Monodisperse emulsion generation via drop break off in a coflowing stream. *Langmuir* **16**, 347–351 (2000).

[55] E. C. Unger, E. Hersh, M. Vannan, T. O. Matsunaga and T. McCreery, Local drug and gene delivery through microbubbles. *Progress in Cardiovascular Diseases* **44**, 45–54 (2001).

[56] Y. Wang and P. Dimitrakopoulos, A three-dimensional spectral boundary element algorithm for interfacial dynamics in Stokes flow *Phys. Fluids* **18**, 082106 (2006).

[57] Y. Wang and P. Dimitrakopoulos, Low-Reynolds-number droplet motion in a square microfluidic channel. *Theor. Comput. Fluid Dyn.* **26**(1-4), 361–379 (2012).

[58] Z. Z. Wong and J. L. Bull, Vascular bubbles and droplets for drug delivery. *J. Drug Del. Sci. Tech.* **21**(5), 2011.

[59] L. Wu, M. Tsutahara, L. S. Kim and M. Ha, Three-dimensional lattice Boltzmann simulations of droplet formation in a cross-junction microchannel. *Int. J. Multiphas. Flow.* **34** 852–864 (2008).

[60] C.S. Yih, Fluid Mechanics, West River Press, (1980).

[61] G. K. Youngren and A. Acrivos, On the shape of a gas bubble in a viscous extensional flow *J. Fluid Mech.* **76**(3), 433–442 (1976).

[62] M. Zagnoni, C. N. Baroud and J. M. Cooper, Electrically initiated upstream coalescence cascade of droplets in a microfluidic flow. *Phys. Rev. E.* **80**, 046303 (2009).

[63] A. Z. Zinchenko and R. H. Davis, A multipole-accelerated algorithm for close interaction of slightly deformable drops. *J. Comp. Phys.* **207**, 695–735 (2005).

Vita

Thomas K. Deskins was born in Baltimore, Maryland. He entered the Department of Chemical and Biomolecular Engineering at the University of Maryland in College Park, Maryland in August 2013. He graduated in May 2017 receiving his Bachelor of Science degree in Chemical Engineering. After receiving his Bachelor's degree, he enrolled in graduate studies at the Department of Chemical and Biomolecular Engineering at the University of Maryland in College Park, Maryland in August 2017. At this same time, he joined the Bio-Fluid Dynamics Laboratory and conducted research on the flow dynamics of droplets in microfluidic expansions under the guidance of Professor Panagiotis Dimitrakopoulos. In July 2018, he defended his thesis for the Master of Science degree, entitled "Droplet dynamics in microfluidic expansions".